ACS APPLIED MATERIALS & INTERFACES

Research Article

Cite This: ACS Appl. Mater. Interfaces 2018, 10, 40661−40671

www.acsami.org

One-Step Co-Evaporation of All-Inorganic Perovskite Thin Films with Room-Temperature Ultralow Amplified Spontaneous Emission Threshold and Air Stability

Lin Zhang,[†] Fang Yuan,[†] Hua Dong,[†] Bo Jiao,[†] Wenwen Zhang,[‡] Xun Hou,[†] Shufeng Wang,*[,§] Qihuang Gong,[§] and Zhaoxin Wu*[,†,∥]

[†]Key Laboratory of Photonics Technology for Information, Key Laboratory for Physical Electronics and Devices of the Ministry of Education, School of Electronic and Information Engineering, Xi'an Jiaotong University, Xi'an 710049, China

[‡]School of Electronic Engineering, Xi'an University of Post & Telecommunication, Xi'an 710121, China

[§]State Key Laboratory for Mesoscopic Physics and Department of Physics, Peking University, Beijing 100871, China

[∥]Collaborative Innovation Center of Extreme Optics, Shanxi University, Taiyuan 030006, China

Supporting Information

ABSTRACT: Inorganic cesium lead halide perovskite has been successfully applied in the optoelectronic field due to its remarkable optical gain properties. Unfortunately, conventional solution-processed $CsPbX_3$ films suffer unavoidable pinhole defects and poor surface morphology, severely limiting their performance on amplified spontaneous emission (ASE) and lasing applications. Herein, a dual-source thermal evaporation approach is explored to achieve a uniform and high-coverage $CsPbX_3$ polycrystalline thin film. It was found that one-step co-evaporated $CsPbBr_3$ (OC-$CsPbBr_3$) thin films without post-annealing exhibit an ultralow ASE threshold of ~3.3 $\mu J/cm^2$ and a gain coefficient above 300 cm^{-1}. The coexistence of cubic and orthorhombic phases in these materials naturally form an energy cascade for the exciton transfer process, which enables rapid accumulation of excitons. Stable ASE intensity without degradation for at least 7 h is also realized from OC-$CsPbBr_3$ thin films under continuous excitation, which is superior to that in the solution-processed $CsPbBr_3$ thin films. Notably, a Fabry−Pérot cavity laser based on the OC-$CsPbBr_3$ thin film is first achieved, featuring an ultralow lasing threshold (1.7 $\mu J/cm^2$) and directional output (a beam divergence of ~3.8°). This work highlights the noteworthy optical properties of OC-$CsPbBr_3$ thin films, leading to potential available applications in integrated optoelectronic chips.

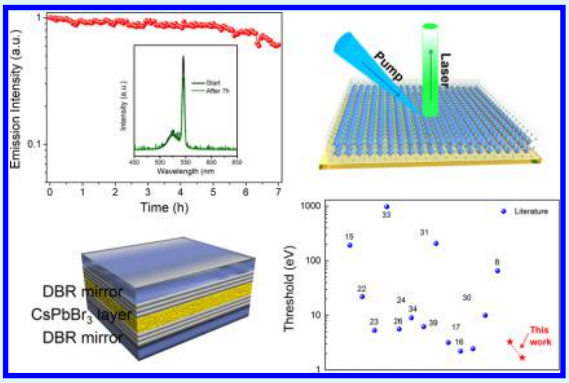

KEYWORDS: *cesium lead halide perovskite, thin films, vapor deposition, amplified spontaneous emission, long-term stability*

1. INTRODUCTION

Recently, organic−inorganic halide perovskites such as $MPbX_3$ (M = methylammonium (MA) or formamidinium (FA), X = Cl, I, Br) have emerged as the attractive new generation of photonic materials, especially with their record of certified research solar cells showing power conversion efficiencies up to 22.7%.[1−10] Such perovskites also have great potential for wide-ranging applications in light emission, owing to their high charge-carrier mobility, tunable band gap, low trap density, high-photoluminescence quantum yield, and high defect tolerance.[11−14] However, the intrinsic volatility of organic components against moisture sensitivity and their low thermal stability remains an impediment for realizing the practical and commercial applications.[15,16] Alternatively, all-inorganic perovskites show improved endurance under ambient conditions compared with organic hybrid perovskites. In addition, their unique optoelectronic properties further promote their applications in colorful light-emitting diodes (LEDs), optically pumped amplified spontaneous emissions (ASE), and lasers.[17−27] On account of the remarkable optical gain features of perovskite materials, some studies chiefly focused on the low-threshold ASE and lasing in $CsPbX_3$ perovskites, or assembling $CsPbX_3$ perovskites with external optical cavity configurations to achieve a coherent laser output, such as the surface-emitting vertical Fabry−Pérot (F−P) cavity and distributed feedback gratings.[28−34]

Despite the progressive understanding of the gain media with integrated external optical cavities, most of the gain media are concentrated on inorganic $CsPbX_3$ nanocrystals. Considering the complex manufacture process of perovskite nano-

Received: September 13, 2018
Accepted: November 5, 2018
Published: November 5, 2018

DOI: 10.1021/acsami.8b15962
ACS Appl. Mater. Interfaces 2018, 10, 40661−40671

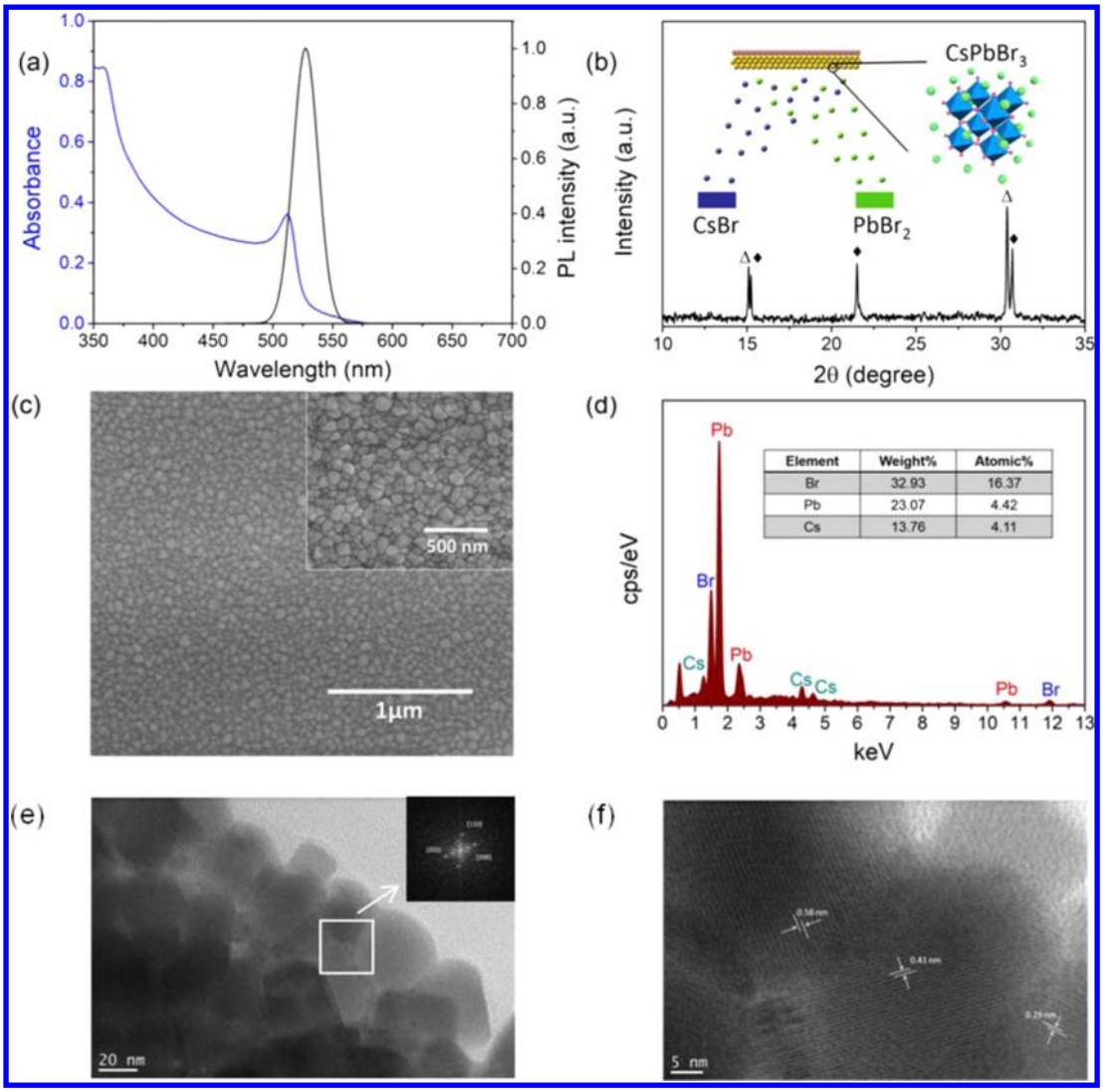

Figure 1. OC-$CsPbBr_3$ thin film is obtained. (a) The normalized UV−visible absorbance and PL emission spectra of the OC-$CsPbBr_3$ thin film. (b) Measured XRD pattern of the OC-$CsPbBr_3$ thin film, which is interpreted as the mixture of orthorhombic (Δ) and cubic (♦) lattices. (c) Top-view scanning electron microscopy images of the OC-$CsPbBr_3$ thin film, 25 °C, represent the film without post-annealing. (d) EDS spectrum of the OC-$CsPbBr_3$ thin film, showing a clear elemental composition. (e) TEM image and (f) HRTEM image of the OC-$CsPbBr_3$ thin film.

crystals, however, $CsPbX_3$ thin films have the advantages of a simpler synthesis route and desirability in integrated optoelectronic chips. It is known that compact and smooth perovskite polycrystalline thin films are crucial to compensate the short optical gain length to provide sufficient gain for realizing ASE enhancement. As for the solution-processed perovskite thin films, such as those manufactured by the spin-coating or thermal spraying method, the crystallization process is relatively sensitive to the experimental condition. Meanwhile, the low solubility of the inorganic cesium salt (CsBr and CsI) inevitably leads to poor element distribution and poor surface coverage,[35−38] limiting the realization of commercially available perovskite-based optoelectronics.[39−43] However, the perovskite thin films fabricated by dual-source thermal evaporation present desirable advantages with regard to film morphology and surface coverage,[44−49] whose reliable long-term stability greatly benefits the operational stability of the devices.[50,51] This approach offers a potential substitute to improve the performance of the ASE or lasing in $CsPbX_3$ thin films.

In this case, we developed a facile co-evaporation method to prepare the $CsPbBr_3$ thin films. The $CsPbBr_3$ thin film without post-annealing is named as the OC-$CsPbBr_3$ thin film. The OC-$CsPbBr_3$ thin films not only exhibit a compact and smooth surface morphology, but also remedy the inhomogeneous element distribution in solution-processed $CsPbBr_3$ thin films. Based on the Volmer−Weber growth mode, we tentatively propose a reaction mechanism for the growth of the co-evaporated $CsPbBr_3$ thin film. At low evaporation rates, two precursor molecules possess low kinetic energy and can more easily react with each other, and then undergo crystal growth. Meanwhile, the perovskite thin films prepared via the thermal evaporation process with a high substrate temperature exhibit a particular feature of two-phase crystal structure.[52,53] The two-phase coexistence in OC-$CsPbBr_3$ thin films is beneficial to establish an energy cascade for the exciton transfer process, which helps realize the build-up of population inversion. Here, the OC-$CsPbBr_3$ thin films exhibit an ultralow ASE threshold of ∼3.3 $\mu J/cm^2$ and optical gain above 300 cm^{-1}. As for their long-term stability, the OC-$CsPbBr_3$ thin films maintain the ASE efficiency after 10 days of storage under ambient

DOI: 10.1021/acsami.8b15962
ACS Appl. Mater. Interfaces 2018, 10, 40661−40671

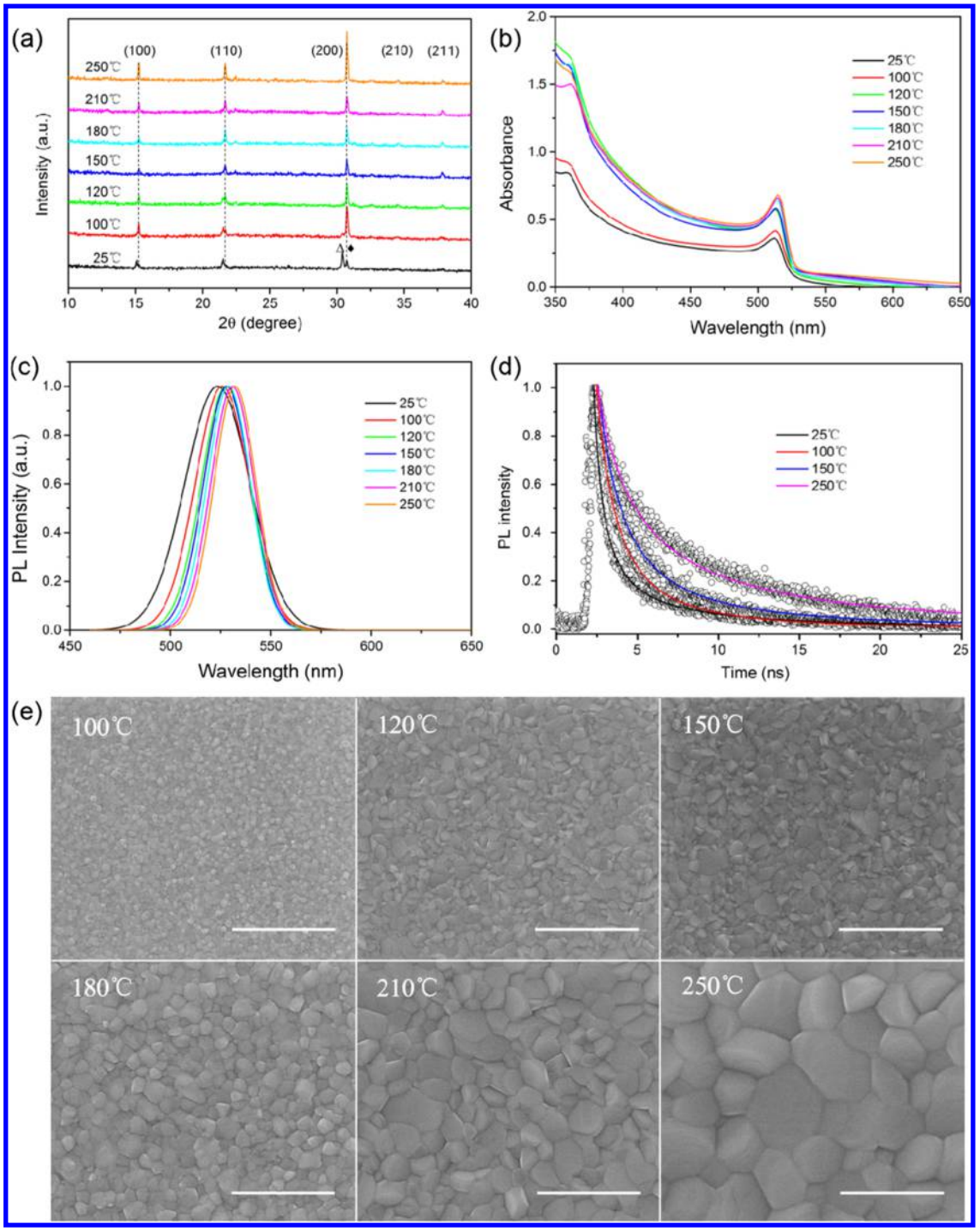

Figure 2. (a) A series of measured XRD patterns of unannealed or annealed $CsPbBr_3$ thin films (post-annealing temperature range from 100 to 250 °C, and 25 °C represents the unannealed film). The orthorhombic (Δ) and cubic (♦) phase peaks coexist in the crystal pattern of the OC-$CsPbBr_3$ thin film. (b) The UV−visible, (c) PL emission spectra, (d) time-resolved PL spectra, and (e) top-view scanning electron microscopy images of the $CsPbBr_3$ thin films. Scale bar: 1 μm.

conditions (25 °C, 50% RH). Upon continuously pumping (~7 h) at room temperature, 90% of the initial ASE intensity is mostly retained in OC-$CsPbBr_3$ thin film compared with only 9% of the initial ASE value in the solution-processed thin films. Furthermore, the Fabry−Pérot (F−P) cavity laser based on OC-$CsPbBr_3$ thin films is realized with an ultralow lasing threshold (~1.7 $\mu J/cm^2$) and high beam quality output signal (~3.8°). Our results highlight the noteworthy optical properties of OC-$CsPbBr_3$ thin films, and present a compelling direction for the realization of on-chip coherent light sources.

2. EXPERIMENTAL SECTION

2.1. Preparation of the Perovskite Thin Film. The glass/indium tin oxide substrates were cleaned sequentially by ultrasonication with a cleaner solution, acetone, alcohol, distilled water, and isopropyl alcohol, followed by UV−ozone treatment for 5 min prior to use. The precursors cesium bromide (CsBr) and lead bromide ($PbBr_2$) were loaded in two independent crucibles and the

DOI: 10.1021/acsami.8b15962
ACS Appl. Mater. Interfaces 2018, 10, 40661−40671

sample substrates were placed in a rotatable substrate holder facing toward the precursor sources, and after the pressure of the evaporator chamber was pumped down to 10^{-6} mbar, the two precursors were deposited at the rate of 0.50 and 0.54 Å/s, respectively, to achieve a molar ratio of 1:1 until the thickness was reached. An appropriate deposition rate is beneficial to ensure maximal packing density and morphology within a reasonable deposition period. During the process, two quartz crystal microbalances monitored the deposition rate of the two precursors on the sample. Right after the thermal deposition, the freshly grown $CsPbBr_3$ samples were heated at X °C for 2 min each (X = 100, 120, 150, 180, 210, and 250) under ambient conditions. These $CsPbX_3$ perovskite films containing pure and mixed halides were prepared with the desired thicknesses of PbX_2 and CsX of about equal stoichiometric ratio. As for the control sample of solution-processed $CsPbBr_3$ thin film, the precursor solution was synthesized by adding an equimolar ratio of $CsBr/PbBr_2$ (0.3 mmol) in 1 mL dimethyl sulfoxide solvent, and then dissolved at 60 °C for 30 min and stirred for 6 h at room temperature, spin-coated with 500 μL $CsPbBr_3$ solution (3000 rpm for 40 s) by a one-step method onto the substrate in a glovebox, and at 20 s before the last spin-coating, 80 μL chlorobenzene solvent was dropped quickly onto the substrate. Then, the freshly grown $CsPbBr_3$ thin film was annealed at 100 °C for 10 min.

2.2. Fabrication of the $CsPbBr_3$-Based Fabry–Pérot Cavity. The DBRs were cleaned by ultrasonication with a cleaner solution, acetone, alcohol, distilled water, and isopropyl alcohol to ensure no attached particles. The perovskite layer was directly evaporated onto DBR substrates by double-source thermal evaporation. Then, these DBRs were bound together with a certain pressure to minimize the gap in cavity and fixed with glue.

2.3. Characterization. The film thickness of the samples was measured by ellipsometry (SEMF-1000, Korea). The surface of the $CsPbX_3$ thin films was investigated by scanning electron microscopy (SEM, Quanta 250, FEI). The surface topography of the $CsPbX_3$ thin films was measured by an atomic force microscope (AFM, NT-MDT, Russia). Transmission electron microscopy was carried out with a JEM-2100F TEM (JEOL, Japan) operating at a beam energy of 200 keV. The crystalline structure of the $CsPbBr_3$ thin films on a glass substrate was determined by X-ray diffraction (XRD, D/MAX-2400, Rigaku, Japan). The absorption and PL spectra were obtained by a UV–vis spectrophotometer (HITACHI U-3010, Japan) and a fluorescence spectrometer (Fluoromax-4 spectrofluometer), respectively. The femtosecond pulses were delivered from a Ti:sapphire femtosecond laser (400 nm excitation wavelength, 150 fs pulse width, 1 kHz repetition rate). The nanosecond pulses were delivered by a Nd:YAG laser (355 nm excitation wavelength, 5.5 ns pulse width, 10 Hz repetition rate). The effective refractive index of the perovskite was measured with a variable angle spectroscopic ellipsometer (J. A. Woollam M-2000DI). The scanning PL mapping of the $CsPbBr_3$ thin film on the glass substrate was determined by a Laser Raman Spectrometer (HORIBA LabRAM HR Evolution-800) (325 nm laser with power below 2.5 mW). All PL spectra are the aggregation containing 10 000 PL data collected from setting up 0.5 μm as the step size. Face emission spectra were collected by a fiberoptic spectrometer (Ocean Optics Spectra Suite, USB2000). The distance between the samples and fiber was set as 20 mm, and combined with a charge-coupled device (CCD) detector. All measurements were carried out under ambient conditions at room temperature.

3. RESULTS AND DISCUSSION

3.1. Characterization of $CsPbBr_3$ Perovskite Films. As described in the Experimental Section, the $CsPbBr_3$ thin films were co-evaporated directly onto the glass substrates with the same molar quantity of precursor materials. Figure 1a shows the photoluminescence (PL) and absorption spectra of a 200 nm OC-$CsPbBr_3$ thin film. The PL peak and absorption edge are located at around 525 and 515 nm, respectively, corresponding to the excitonic recombination near the edges of the direct band gap.[54] The X-ray diffraction (XRD) pattern of OC-$CsPbBr_3$ thin films is shown in Figure 1b. The diffraction peaks are located at 15.24, 21.67, and 30.71°, indexing to (100), (110), and (200) planes of the cubic phase. In addition, the peaks split at 15.16 and 30.28° are consistent with the orthorhombic phase. Regardless of the radio between the cubic and orthorhombic phases, the two-phase coexistence in OC-$CsPbBr_3$ is a particular feature of dual-source thermal evaporation. Meanwhile, the OC-$CsPbBr_3$ thin films exhibit ultralow surface roughness (RMS = 2.17 nm) and a pinhole-free morphology (Figures 1c and S1). The energy dispersion spectroscopy (EDS) result shows Pb/Cs and Br/Pb molar ratios of about 1.0 and 3.7 respectively, agreeing well with the stoichiometric ratio (Figure 1d).[55] The transmission electron microscopy (TEM) images of some particles scraped from the as-prepared OC-$CsPbBr_3$ thin film are presented in Figure 1e. Based on the XRD patterns and TEM electron diffraction patterns (Figure 1e, insets), these two types of crystalline grains are mixed uniformly in the microperspective. The high-resolution lattice with an interplanar spacing of d = 0.41 nm is consistent with the (110) crystal plane of the cubic phase, whereas the d = 0.58 nm is consistent with the (202) crystal plane of the orthorhombic phase, further confirming the two-phase coexistence property of the OC-$CsPbBr_3$ thin film.[56]

Besides, we applied the laser Raman optical imaging technique on OC-$CsPbBr_3$ thin films for intuitively identifying the PL intensity and uniformity, as shown in Figure S2. We also prepared solution-processed $CsPbBr_3$ (S-$CsPbBr_3$) thin films via one-step spin coating for comparison. The PL peaks of both thin films are located at 525 nm with similar full width at half-maximum (FWHM) of 18 nm. In Figure S2c–f, the OC-$CsPbBr_3$ thin film displays a bright and uniform PL emission distributed across the surface, proving the uniform element distribution and excellent surface coverage. However, the solution-processed thin film shows inhomogeneous element distribution and PL emission, probably caused by incomplete surface coverage and high roughness.

A post-annealing process is generally used to induce phase transition and control the morphology to realize high-quality perovskite thin films. Hence, the optical properties and crystallinities of co-evaporated $CsPbBr_3$ thin films under different post-annealing temperatures were also investigated. As shown in Figure 2a, the XRD spectra show a gradual transition into the cubic phase as the post-annealing temperature increases. Moreover, the shift of the absorption edge and PL peak also reveal a lower band gap of the perovskite form (Figure 2b,c). Due to the decrease of the Pb–Br bond angle in orthorhombic perovskite, the lower band dispersion of the valence band around the gap points toward the higher energy gap.[57] Compared with annealed thin films, the two-phase coexistence in the OC-$CsPbBr_3$ thin film will naturally form an energy cascade, enabling the exciton transfer process from higher energy-gap (orthorhombic-phase) composites to lower energy-gap (cubic-phase) composites.[58] The PL quantum yields (QY) of the perovskite thin films were also measured, and a relatively low value of ~5.6% for the OC-$CsPbBr_3$ thin film was obtained, whereas the 250 °C annealed $CsPbBr_3$ thin film exhibits a higher PLQY (12.2%). Figure 2d shows that the corresponding PL lifetime of the annealed $CsPbBr_3$ thin film is larger than that of the OC-$CsPbBr_3$ thin film. The longer PL lifetime of annealed thin films indicates less nonradiative recombination channels as compared with OC-$CsPbBr_3$ thin films. Considering that there is no direct correlation between

DOI: 10.1021/acsami.8b15962
ACS Appl. Mater. Interfaces 2018, 10, 40661–40671

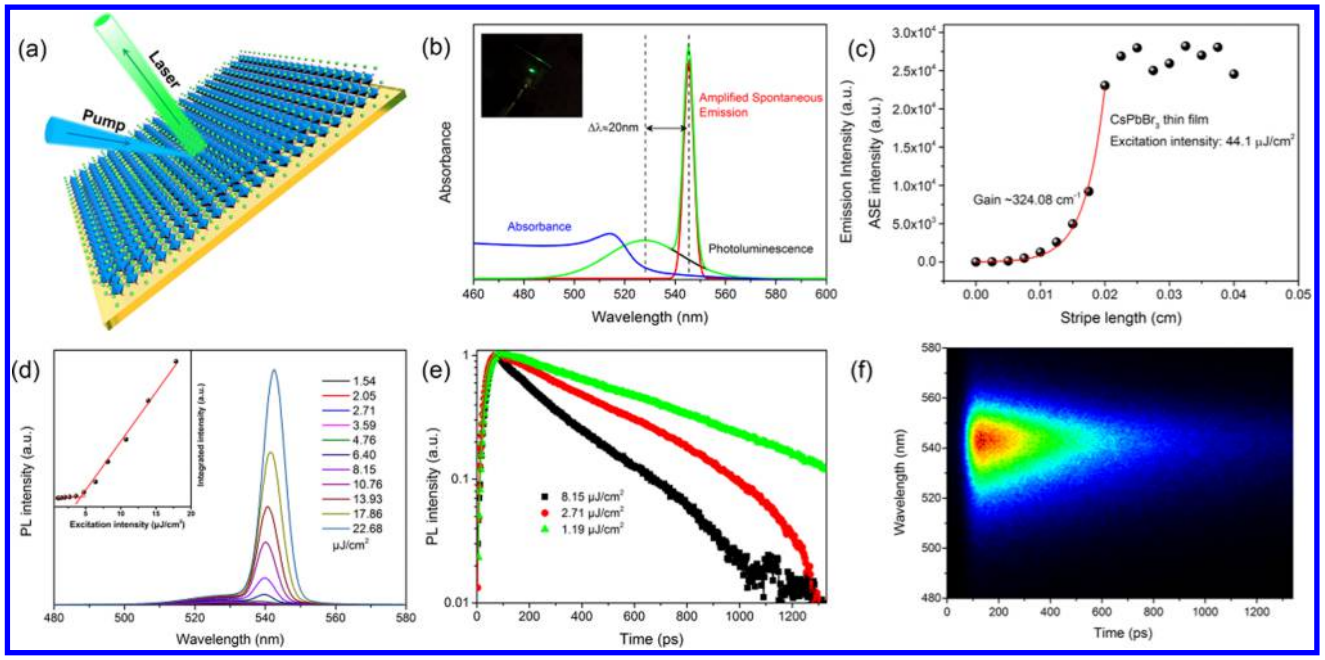

Figure 3. Amplified spontaneous emission from femtosecond pulsed excitation in the OC-$CsPbBr_3$ thin film. (a) Schematic of the OC-$CsPbBr_3$ thin film. (b) A comparison of the amplified spontaneous emission profile (red) in relation to the absorption (blue) and spontaneous emission (black) profiles of the OC-$CsPbBr_3$ thin film in a normalized scale. Inset: the real color optical image of the OC-$CsPbBr_3$ thin film excited above the ASE threshold. (c) Variable stripe-length experiment for estimation of the optical gain of the OC-$CsPbBr_3$ thin film. The spectra is excited at λ = 355 nm with nanosecond laser pulses. The red line is the best-fitting curve based on the variable stripe length method. (d) Development of a spectrally narrow amplified spontaneous emission with increasing pump intensity. (e) Time-resolved PL decay dynamics of the OC-$CsPbBr_3$ thin film following photoexcitation with the pumping intensity below (blue), close to (red), and above (black) the ASE threshold value. (f) Streak camera images of the PL spectrum vs time (collected over a time window of ~1340 ps) under a pump intensity above the ASE threshold value.

the PLQY and ASE threshold, we exclude relevant roles of trapping processes to affect the ASE properties of $CsPbBr_3$ polycrystalline thin films.[59]

The scanning electron microscopy (SEM) (Figure 2e) and atomic force microscopy (AFM) (Figure S3) images of annealed $CsPbBr_3$ thin films confirm that the post-annealing process drives grain growth continually and the adjacent grains are then merged into bigger ones, thus leading to the higher surface roughness. In the context of optical gain materials, a rougher surface will decrease the intensity of light oscillation within the thin film and increase the proportion of the escaping light at the air−film interface, which may be harmful for the creation of ASE, leading to low ASE efficiency.[60]

3.2. ASE Intensity from $CsPbBr_3$ Perovskite Film. To evaluate the ASE efficiency of OC-$CsPbBr_3$ thin films, the thin films were excited at 400 nm by a frequency-doubled Ti:sapphire femtosecond laser oscillator delivering 150 fs pulses at a 1 kHz repetition rate. All measurements were carried out under ambient conditions at room temperature. Lasing from effective optical feedback provided by light oscillation in optical gain materials and sufficient thickness of thin films is needed for a high-efficiency optical output.[61] Figure 3a schematically displays the oscillated light among the $CsPbBr_3$ crystals in thin films under pump light excitation, where a sharp ASE peak can be observed consequently. From the contrast spectra of PL (black) and ASE (red) of the OC-$CsPbBr_3$ thin film in a normalized scale (Figure 3b), it can be observed that above the threshold, the ASE peak is red-shifted by ~20 nm with respect to the PL maximum. Because of the strong self-absorption during exciton lasing or in the exciton binding energies in the bi-exciton optical gain mechanism, the ASE peak red shifts where the optical gain and absorption are balanced.[62−64] The optical gain of a material is an important figure-of-merit that indicates the performance of light amplification for achieving lasing. The optical gain coefficient of OC-$CsPbBr_3$ thin film is estimated by the standard variable stripe length (VSL) methods (Figure 3c). The exponential data are fitted using eq 1

$$I_{ASE}(L) = (A/g)[\exp(gL) - 1] \quad (1)$$

where I_{ASE}, A, g, and L are the detected ASE intensity, the cross-sectional excited area mapped by the penetration depth, gain coefficient, and excitation stripe length, respectively.[65] The estimated gain coefficient of the OC-$CsPbBr_3$ thin film is to be ~324 cm^{-1}. The measured output emission spectra and input−output intensity as a function of increasing excitation intensity of OC-$CsPbBr_3$ thin films are shown in Figure 3d. The ASE increases rapidly over the narrow peak with respect to the pump intensity, which confirms the development of stimulated emission. It reveals clear signatures of the ASE behavior, showing spectral narrowing of the emission peaks and a steep rise of the emission intensity under an excitation intensity above the threshold, where the estimated pumped intensity is around 3.3 $\mu J/cm^2$. Time-resolved PL dynamics as a function of pump intensity is regarded as a common tool to characterize the expected feature of ASE. Figure 3e shows the time-resolved PL measurement of the OC-$CsPbBr_3$ thin film optically pumped of $0.4P_{th}$, $0.8P_{th}$, and $2.5P_{th}$ (P_{th} is the ASE threshold pump intensity) under ambient conditions. Well above the ASE threshold, the typical ASE lifetime of approximately 1100 ps was observed. Such a fast decay process with increased pump intensity could be ascribed to the nonradiative decay channel. Figure 3f shows the time-resolved PL spectrogram obtained using a streak camera. The

DOI: 10.1021/acsami.8b15962
ACS Appl. Mater. Interfaces 2018, 10, 40661−40671

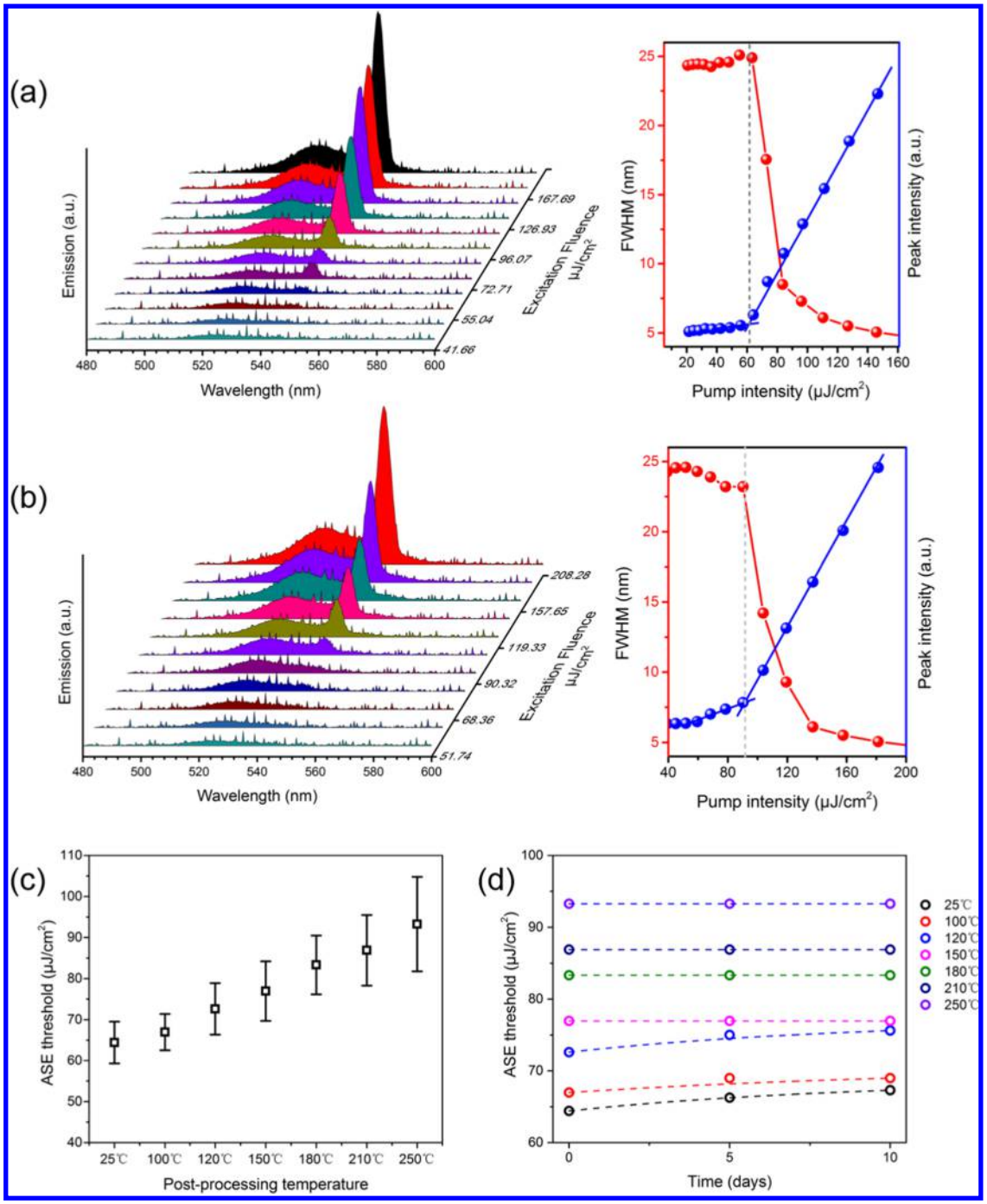

Figure 4. Amplified spontaneous emission from nanosecond pulsed excitation in $CsPbBr_3$ thin films. The emission spectra, output intensity, and FWHM as a function of pumping density for (a) OC-$CsPbBr_3$ and (b) 250 °C annealed $CsPbBr_3$ thin films. (c) ASE threshold values of freshly prepared $CsPbBr_3$ thin films after different post-processing temperatures. Each data point is collected from five films. (d) Corresponding ASE threshold values for freshly prepared $CsPbBr_3$ thin films and 10 days later, respectively.

predominantly rapid decay at an emission wavelength of 545 nm reflects a stimulated emission process, providing further evidence of the ASE of the OC-$CsPbBr_3$ thin film. The fast nonradiative recombination manifests as the bright stripe in the spectrogram. Such an ultralow ASE threshold and high gain value suggest that the OC-$CsPbBr_3$ thin film could be a promising candidate for laser fabrication. Our results emphasize that the potential of the one-step co-evaporation process to fabricate high-quality perovskite films supersedes the solution-processed method, offering a route to design novel, highly stable thin films for efficient optoelectronics, such as highly integrated on-chip perovskite lasers.

To further investigate the potential for a "quasi-continuous wave" regime of excitation, the $CsPbBr_3$ thin films pumped by a frequency-doubled Nd:YAG laser (355 nm, 5.5 ns, 10 Hz) were obtained. As shown in Figure 4, the gain-induced bandwidth narrowing and the threshold behavior in emission intensity indicated that the SE transforms into ASE. In case of the OC-$CsPbBr_3$ thin film, an obvious transition in the gradient of the PL intensity curve and a sharp decrease in the full width half-maximum (FWHM) occurred as the optical

DOI: 10.1021/acsami.8b15962
ACS Appl. Mater. Interfaces 2018, 10, 40661−40671

pumping intensity gradually increased. A kink is observed from the emission vs pump intensity curve at an optical excitation intensity equal to 64.9 $\mu J/cm^2$, whereas that of the 250 °C annealed $CsPbBr_3$ thin film can be up to 93.2 $\mu J/cm^2$ (Figure 4b). Due to the changes in the film morphology, the occurrence of low ASE thresholds is correlated to the degree of perovskite crystallinity, which is similar to the case with mixed-dimensional bromide-based perovskites.[66] Figure 4c shows that the ASE threshold of $CsPbBr_3$ thin films is increased as the post-annealing temperature rises, confirming that the ASE acts in relation to the surface morphology and crystallinity of thin films. Moreover, the co-evaporated $CsPbBr_3$ thin film displays superb photochemical and structural stability after 10 days of storage under ambient conditions (25 °C, 50% RH) (Figures 4d and S4), indicating them as suitable gain media in coherent light sources. In addition, the estimated ASE threshold of the S-$CsPbBr_3$ thin film is 0.487 mJ/cm^2 (Figure S5), which is about 7.6-fold higher than that of the OC-$CsPbBr_3$ thin film. These findings indicate the potential for employing OC-$CsPbBr_3$ thin films for the realization of continuous-wave (CW) pumped lasers and provide an effective route for the synthesis of high-quality thin films with a large optical gain.

3.3. Mechanism of ASE Induced by the Two-Phase Coexistence Characteristic. Under the increased pump intensity, the generated photons of spontaneous emission of optical gain media are amplified by stimulated emission and undergo the optical gain phenomenon induced by intrinsic disorder in perovskites. Consequently, the sharp emission peak of lasing can be observed from the thin films.[37] Therefore, the oscillation light path and film morphology of optical gain materials are the key points for enhancing the ASE intensity. Table S1 summarizes the recent key parameters of ASE/lasing from $CsPbBr_3$ perovskite gain media. Notably, the gain coefficient, stability, and threshold of OC-$CsPbBr_3$ thin films approach the values reported for nanocrystal gain media. The analysis of the XRD peak positions reveals that the orthorhombic and cubic phases coexist in the OC-$CsPbBr_3$ thin films. Compared with self-organized multiple quantum wells observed in quasi-2D perovskites, the multiphase structure of pure 3D perovskite builds an energy cascade for exciton transfer.[66] We propose that the improved ASE efficiency may be due to the grain boundary or phase-separation effect that leads to an improvement in multiple random scattering. As shown in Figure S6, the coexistence of two phases in OC-$CsPbBr_3$ thin films might form an energy cascade for the exciton transfer process from higher-energy gap composites to lower-energy gap composites, as deduced from two aspects. On the one hand, the band gaps of the OC-$CsPbBr_3$ and the annealed $CsPbBr_3$ thin films are calculated to be 2.40 and 2.34 eV from absorption data using the Tauc relation, respectively. On the other hand, from the density functional theory (DFT) calculations of the band structures for the $CsPbBr_3$ thin film, the calculated band gap for the cubic-phase $CsPbBr_3$ is about 2.26 and it increases to 2.49 eV for orthorhombic-phase $CsPbBr_3$. This trend is in agreement with the experimentally determined gaps. As the exciton populations increase, a part of the photoexcited excitons transfer from orthorhombic phase to the cubic phase, leading to rapid accumulation of excitons. This effectively establishes a population inversion for achieving ASE. Moreover, the slope of the exponential part of the absorption coefficient curve shows an unusual sharp shoulder. The smaller Urbach energy measured here for annealed $CsPbBr_3$ thin films indicates lesser disorder and narrower distribution of states near the band edge, which coincides with the supposition of the exciton transfer process. Besides, the OC-$CsPbBr_3$ thin films display more compact and smaller crystal grains than annealed $CsPbBr_3$ thin films, indicating that the smoother surface morphology is beneficial for reducing the optical loop distance and contributes to ASE enhancement.

3.4. Long-Term Ability and Wavelength Tunability of ASE. The long-term stability of OC-$CsPbBr_3$ thin films is assessed by monitoring the ASE intensity as a function of operation time under a continuous laser pulse, as shown in Figure S7. A nearly constant ASE intensity (90% of the initial intensity) was observed for the OC-$CsPbBr_3$ thin film under continuous excitation in air for at least 7 h, indicating that OC-$CsPbBr_3$ thin films possess outstanding long-term stability under ambient conditions. The excellent photostability is most likely attributable to the superb structural and photochemical performance in the high-quality co-evaporated $CsPbBr_3$ thin film, and we believe that our films can find potential applications as suitable gain media with integrating resonant cavities for strong coherent light emission. For comparison, the ASE intensity in the S-$CsPbBr_3$ thin films decreased to 9% of the initial value after continuous pumping. Solution-processed halide perovskite thin films suffer from imperfect stability owing to their solution process, which can easily possess a high concentration of surface defects, and their sensitivity to moisture and light.[67] Moreover, a higher ASE threshold in S-$CsPbBr_3$ thin films will produces larger joule heating than co-evaporated thin films, which may reduce their photostability performance significantly.[32] Such results further indicate that co-evaporation can protect samples from damaging under continuous and high-intensity excitation. By controlling the relative constituent stoichiometry of halides during the synthesis process, the emission wavelength of the perovskite thin film displays excellent tunability from the green to red region; the PL and ASE wavelengths of $CsPb(Br/I)_3$ thin films can be found in Figure S8. Notably, the ASE threshold of the $CsPbBr_2I$ thin film is as low as 14.54 $\mu J/cm^2$ (17.04 and 12.66 $\mu J/cm^2$ for $CsPbBrI_2$ and $CsPbI_3$ samples, respectively). These results unravel that thin films from our method display highly desirable PL/ASE characteristics, which is especially important in the practical application. Due to the well-known phenomenon of phase segregation in mixed halides' compositions under continuous light illumination, our work mainly presents the photostability of $CsPbBr_3$ thin films.

3.5. OC-$CsPbBr_3$ Film-Based Fabry–Pérot Optical Cavity. As one systematic study based on the lasing applications reported, the resonator laser emission also can be achieved by a suitable cavity resonator with perovskites as distributed feedback lasing. The uniform PL intensity and high ASE efficiency of the OC-$CsPbBr_3$ thin films prompt us to embed such samples into a cavity resonator, which is particularly attractive for the realization of on-chip coherent light sources. Herein, we choose the OC-$CsPbBr_3$ thin film as the optical gain media for a typical F–P optical cavity design, sandwiched by two high-reflectivity mirrors parallel to each other. We investigated the lasing from the resonant cavity under Ti:sapphire femtosecond pulsed excitation. To explore the cavity effect of light oscillation and amplification, here we directly deposited about 270 nm OC-$CsPbBr_3$ thin film onto the surface of two DBRs to increase the optical gain length. Next, we put these two DBRs together and fixed them with

DOI: 10.1021/acsami.8b15962
ACS Appl. Mater. Interfaces 2018, 10, 40661–40671

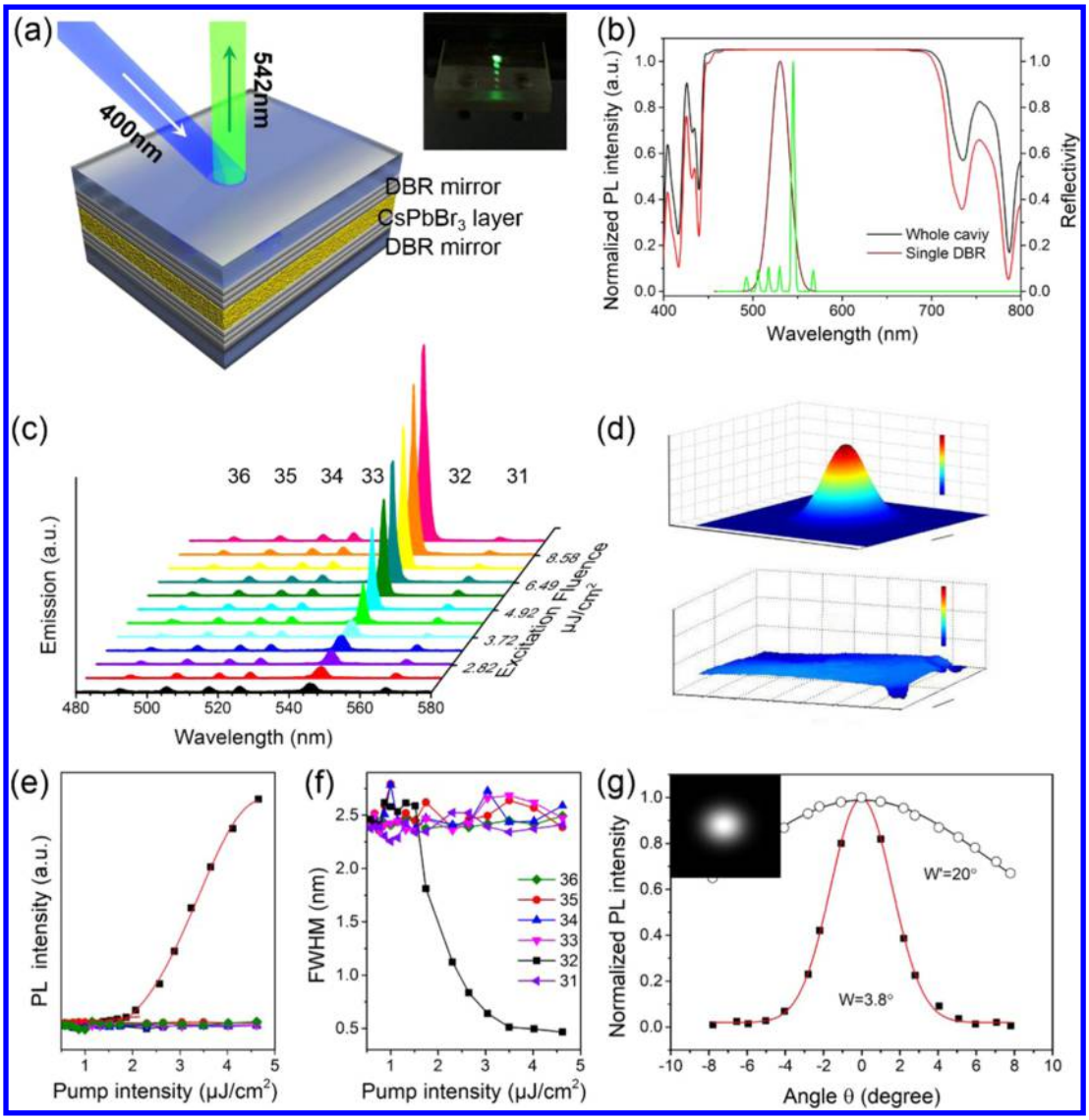

Figure 5. Optical cavity based on the OC-$CsPbBr_3$ thin film. (a) Schematic configuration of the $CsPbBr_3$-based cavity. Inset shows the corresponding photograph of the device in operation. (b) Normalized PL spectrum from the OC-$CsPbBr_3$ thin film without DBR cavity (brown line) and emission spectrum from the perovskite-based cavity (green line) under an excitation intensity of 4.3 $\mu J/cm^2$. Reflection spectra from a single DBR mirror (red line) and a whole cavity made from double DBR mirrors parallel to each other (black line). (c) Emission spectra from the perovskite-based cavity below and above the lasing threshold, revealing the development of stimulated emission. (d) The output beam profiles above (upper one) and below (lower one) the threshold. Scale bar is 1 mm. (e) Pump-intensity-dependent PL intensity and (f) FWHM of the cavity modes indexed from 31 to 36. (g) Spatial distribution of the output emission via angle-resolved PL measurement under a pump intensity of $0.5P_{th}$ and $1.2P_{th}$. Inset shows the far-field image of the emission from the device.

glue to seal the optical cavity. The schematic diagram and photograph of the final device are presented in Figure 5a, where the inset shows a photograph of the device in operation emitting green light.

Before designing the perovskite-based optical cavity, we also performed variable-angle spectroscopic ellipsometer to collect the refractive index of perovskite thin films, about 2.4 at the range-of-interest emission region from the fitting. A credible result of a high refractive index should be derived from compact crystal grains in pinhole-free and smooth polycrystalline thin film. As shown in Figure 5b, in contrast to the PL spectrum from OC-$CsPbBr_3$ thin film on glass, the uniformly spaced resonant peaks in the cavity confirmed the effect of the F−P cavity. It can be noticed that the lasing peak is still located at the red side of the spontaneous emission spectrum of the OC-$CsPbBr_3$ thin film, in accordance with the fact of optical transition.[26] The reflection spectrum of commercially available DBR microcavity used here exhibits >99.9% reflectivity in the wavelength region of 450−700 nm, matching with the absorption and emission spectrum. The high-reflection mirror is essential to counteract the short optical gain length in the resonator cavity. Figure 5c presents intensity-dependent emission spectra of the $CsPbBr_3$-based optical cavity. These emission peaks can be distinguished from 31 to 36 by eq 2

$$m = 2nL/\lambda \tag{2}$$

where m is the mode number, λ is the emission wavelength at the mode number, n is the refractive index of the OC-$CsPbBr_3$ thin film around the emission wavelength, and the effective cavity length L is estimated to be ∼4 μm.[68] A narrow resonant peak located at 542 nm with an FWHM of ∼0.51 nm after the pump intensity exceeded a certain value. The spectra narrow

DOI: 10.1021/acsami.8b15962
ACS Appl. Mater. Interfaces 2018, 10, 40661−40671

sharply in FWHM and the nonlinear increase of the spectrally integrated PL intensity over the narrow peak with respect to the excitation intensity confirm the development of stimulated emission in the $CsPbBr_3$-based optical cavity. After fitting the input−output curve data (the transition "kink" from spontaneous emission to stimulated emission), the estimated lasing threshold appears at the pumping intensity (P_{th}) ∼1.7 $\mu J/cm^2$ under ambient conditions. The directionality of the output signal above (2.1 $\mu J/cm^2$) and below (1.4 $\mu J/cm^2$) the lasing threshold located 20 mm away from the device (Figure 5d) as well as the far-field image of the output beam (inset in Figure 5g) were obtained by a CCD camera. Under a pump intensity lower than the threshold, the emission is blocked within the cavity. A sudden increase of the PL intensity and narrowing of the emission peak indicate the achievement of lasing action. As shown in Figure 5g, a directional emission was obtained when the pump intensity was above the threshold ($1.2P_{th}$), and the divergence of the output signal decreased from 20° for emission below P_{th} to 3.8°. These results confirm the formation of F−P mode oscillation within the cavity. The ultralow lasing threshold demonstrates that OC-$CsPbBr_3$ thin films equipped with optical cavity can potentially serve as the next-generation perovskite lasers. Our work here just provides a possibility of OC-$CsPbBr_3$ thin films with externally defined resonant cavity. Other device performance of the $CsPbBr_3$-based cavity will be discussed in following researches.

4. CONCLUSIONS

In summary, our results highlight that the OC-$CsPbBr_3$ thin films fabricated by one-step co-evaporation possess excellent optical properties, an ultralow ASE threshold (3.3 $\mu J/cm^2$), long-term stability, and optical gain properties, which may make them ideal candidates for further optoelectronic integration applications. Meanwhile, the two-phase coexistence in this materials naturally enable the exciton transfer process, which is beneficial to establish population inversion. Herein, an ultralow ASE threshold with excellent optical gain is obtained in OC-$CsPbBr_3$ thin films. Most importantly, the Fabry−Pérot cavity based on the OC-$CsPbBr_3$ thin films is realized for the first time, featuring an ultralow lasing threshold (1.7 $\mu J/cm^2$) and directional output (a beam divergence of ∼3.8°). Wavelength-tunable PL and ASE via compositional control (mixed halide Br/I) is reported here, which further demonstrates tunable perovskite lasing in the wider-wavelength region. Studies on the thermal deposition process of all-inorganic perovskite as an attractive material for stable photoelectric light emitters lag behind as a photovoltaic light absorber in solar cells for now. In addition to the attractive ultralow and long-term stable ASE threshold, the uniform PL intensity of OC-$CsPbBr_3$ thin films offers an avenue for engineering further optoelectronic applications. Our findings provide a deep insight into a systematic route to one-step co-evaporated thin films as optical gain media in optical cavity lasers, which is promising for developing widespread optoelectronic applications.

■ ASSOCIATED CONTENT

Supporting Information

The Supporting Information is available free of charge on the ACS Publications website at DOI: 10.1021/acsami.8b15962.

Additional figures, including AFM and cross-sectional SEM of OC-$CsPbBr_3$ thin film, PL mapping of OC-$CsPbBr_3$ and S-$CsPbBr_3$ thin film, AFM images of $CsPbBr_3$ obtained at different annealing temperature, XRD of $CsPbBr_3$ thin film, ASE characterization of S-$CsPbBr_3$ thin film, absorption coefficient and calculated band structure of $CsPbBr_3$, stability characterization of OC-$CsPbBr_3$ and S-$CsPbBr_3$ thin film, and morphology, PL, absorption, ASE characterization of $CsPb(Br/I)_3$ thin film; Table S1 with the representative results of threshold from $CsPbBr_3$ perovskite (PDF)

■ AUTHOR INFORMATION

Corresponding Authors

*E-mail: wangsf@pku.edu.cn (S.W.).
*E-mail: zhaoxinwu@mail.xjtu.edu.cn (Z.W.).

ORCID

Zhaoxin Wu: 0000-0003-2979-3051

Notes

The authors declare no competing financial interest.

■ ACKNOWLEDGMENTS

This work was financially supported by the National Natural Science Foundation of China (Grant Nos. 11574248 and 61875161), National Key R&D Program of China (Grant No. 2016YFB0400702), China Postdoctoral Science Foundation (Grant No. 2016M590947), the Fundamental Research Funds for the Central Universities (Grant No. xjj2016031), the National Natural Science Foundation of China (Grant No. 61505161), the Natural Science Basic Research Plan of Shaanxi Province (Grant No. 2017JM6064), and the Scientific Research Plan Projects of Shaanxi Education Department (Grant No. 17JK0700). The SEM work was performed at the International Center of Dielectric Research (ICDR), Xi'an Jiaotong University, Xi'an, China. We thank Dr. J. Xi at the Global Frontier Center for Multiscale Energy Systems, Seoul National University, for his help in this work. We also thank Yanzhu Dai at the International Center for Dielectric Research (ICDR) for her help in using SEM, and Yu Wang at the Instrument Analysis Center of Xi'an Jiaotong University for her help with PLQY and Raman analysis, and Dr. Zhang at the Instrument Analysis Center for her assistance with TEM.

■ REFERENCES

(1) Tan, H.; Jain, A.; Voznyy, O.; Lan, X.; Fp, G. D. A.; Fan, J. Z.; Quintero-Bermudez, R.; Yuan, M.; Zhang, B.; Zhao, Y.; Fan, F.; Li, P.; Quan, L. N.; Zhao, Y.; Lu, Z. H.; Yang, Z.; Hoogland, S.; Sargent, E. H. Efficient and Stable Solution-Processed Planar Perovskite Solar Cells via Contact Passivation. *Science* **2017**, *355*, 722−726.

(2) Shin, S. S.; Yeom, E. J.; Yang, W. S.; Hur, S.; Kim, M. G.; Im, J.; Seo, J.; Noh, J. H.; Seok, S. I. Colloidally Prepared La-Doped $BaSnO_3$ Electrodes for Efficient, Photostable Perovskite Solar Cells. *Science* **2017**, *356*, 167−171.

(3) Yang, W. S.; Park, B. W.; Jung, E. H.; Jeon, N. J.; Kim, Y. C.; Lee, D. U.; Shin, S. S.; Seo, J.; Kim, E. K.; Noh, J. H.; Seok, S. I. Iodide Management in Formamidinium-Lead-Halide-Based Perovskite Layers for Efficient Solar Cells. *Science* **2017**, *356*, 1376−1379.

(4) NERL, 2017. https://www.nrel.gov/pv/assets/images/effciency-chart.png (accessed: November 2017).

(5) Dong, H.; Wu, Z.; Xi, J.; Xu, X.; Zuo, L.; Lei, T.; Zhao, X.; Zhang, L.; Hou, X.; Jen, A. K. Y. Perovskite Photovoltaics: Pseudohalide-Induced Recrystallization Engineering for $CH_3NH_3PbI_3$ Film and Its Application in Highly Efficient Inverted Planar Heterojunction Perovskite Solar Cells. *Adv. Funct. Mater.* **2018**, *28*, No. 1704836.

DOI: 10.1021/acsami.8b15962
ACS Appl. Mater. Interfaces 2018, 10, 40661−40671

(6) Ran, C.; Xi, J.; Gao, W.; Yuan, F.; Lei, T.; Jiao, B.; Hou, X.; Wu, Z. Bilateral Interface Engineering toward Efficient 2D−3D Bulk Heterojunction Tin Halide Lead-Free Perovskite Solar Cells. *ACS Energy Lett.* **2018**, *3*, 713−721.
(7) Rajagopal, A.; Yao, K.; Jen, A. K. Y. Toward Perovskite Solar Cell Commercialization: A Perspective and Research Roadmap Based on Interfacial Engineering. *Adv. Mater.* **2018**, *30*, No. 1800455.
(8) Gao, K.; Zhu, Z.; Xu, B.; Jo, S. B.; Kan, Y.; Peng, X.; Jen, A. K. Y. Highly Efficient Porphyrin-Based OPV/Perovskite Hybrid Solar Cells with Extended Photoresponse and High Fill Factor. *Adv. Mater.* **2017**, *29*, No. 1703980.
(9) Gao, K.; Xiao, L.; Kan, Y.; Yang, B.; Peng, J.; Cao, Y.; Liu, F.; Russell, T. P.; Peng, X. Solution-processed Bulk Heterojunction Solar Cells Based on Porphyrin Small Molecules with Very Low Energy Losses Comparable to Perovskite Solar Cells and High Quantum Efficiencies. *J. Mater. Chem. C* **2016**, *4*, 3843−3850.
(10) Liang, T.; Xiao, L.; Liu, C.; Gao, K.; Qin, H.; Cao, Y.; Peng, X. Porphyrin Small Molecules Containing Furan- and Selenophene-Substituted Diketopyrrolopyrrole for Bulk Heterojunction Organic Solar Cells. *Org. Electron.* **2016**, *29*, 127−134.
(11) Deschler, F.; Price, M.; Pathak, S.; Klintberg, L. E.; Jarausch, D. D.; Higler, R.; Huettner, S.; Leijtens, T.; Stranks, S. D.; Snaith, H. J.; Atatuere, M.; Phillips, R. T.; Friend, R. H. High Photoluminescence Efficiency and Optically Pumped Lasing in Solution-Processed Mixed Halide Perovskite Semiconductors. *J. Phys. Chem. Lett.* **2014**, *5*, 1421−1426.
(12) Sutherland, B. R.; Hoogland, S.; Adachi, M. M.; Wong, C. T. O.; Sargent, E. H. Conformal Organohalide Perovskites Enable Lasing on Spherical Resonators. *ACS Nano* **2014**, *8*, 10947−10952.
(13) Xing, G.; Mathews, N.; Lim, S. S.; Yantara, N.; Liu, X.; Sabba, D.; Grätzel, M.; Mhaisalkar, S.; Sum, T. C. Low-Temperature Solution-Processed Wavelength-Tunable Perovskites for Lasing. *Nat. Mater.* **2014**, *13*, 476−480.
(14) Zhu, H.; Fu, Y.; Meng, F.; Wu, X.; Gong, Z.; Ding, Q.; Gustafsson, M. V.; Trinh, M. T.; Jin, S.; Zhu, X. Y. Lead Halide Perovskite Nanowire Lasers with Low Lasing Thresholds and High Quality Factors. *Nat. Mater.* **2015**, *14*, 636−642.
(15) Niu, G.; Guo, X.; Wang, L. Review of Recent Progress in Chemical Stability of Perovskite Solar Cells. *J. Mater. Chem. A* **2015**, *3*, 8970−8980.
(16) Rong, Y.; Liu, L.; Mei, A.; Li, X.; Han, H. Beyond Efficiency: the Challenge of Stability in Mesoscopic Perovskite Solar Cells. *Adv. Energy Mater.* **2015**, *5*, No. 1501066.
(17) Lee, J.; Kim, D.; Kim, H.; Seo, S.; Cho, S. M.; Park, N. Formamidinium and Cesium Hybridization for Photo- and Moisture-Stable Perovskite Solar Cell. *Adv. Energy Mater.* **2015**, *5*, No. 1501310.
(18) Yuan, F.; Wu, Z.; Dong, H.; Xi, J.; Xi, K.; Divitin, G.; Jiao, B.; Hou, X.; Wang, S.; Gong, Q. High Stability and Ultralow Threshold Amplified Spontaneous Emission from Formamidinium Lead Halide Perovskite Films. *J. Phys. Chem. C* **2017**, *121*, 15318−15325.
(19) Pan, J.; Sarmah, S. P.; Murali, B.; Dursun, I.; Peng, W.; Parida, M. R.; Liu, J.; Sinatra, L.; Alyami, N.; Zhao, C.; Alarousu, E.; Ng, T. K.; Ooi, B. S.; Bakr, O. M.; Mohammed, O. F. Air-Stable Surface-Passivated Perovskite Quantum Dots for Ultra-Robust, Single- and Two-Photon-Induced Amplified Spontaneous Emission. *J. Phys. Chem. Lett.* **2015**, *6*, 5027−5033.
(20) Zhang, Q.; Su, R.; Liu, X.; Xing, J.; Sum, T. C.; Xiong, Q. High-Quality Whispering-Gallery-Mode Lasing from Cesium Lead Halide Perovskite Nanoplatelets. *Adv. Funct. Mater.* **2016**, *26*, 6238−6245.
(21) Akkerman, Q. A.; Gandini, M.; Di Stasio, F.; Rastogi, P.; Palazon, F.; Bertoni, G.; Ball, J. M.; Prato, M.; Petrozza, A.; Manna, L. Strongly Emissive Perovskite Nanocrystal Inks for High-Voltage Solar Cells. *Nat. Energy* **2016**, *2*, No. 16194.
(22) Dai, J.; Xi, J.; Li, L.; Zhao, J.; Shi, Y.; Zhang, W.; Ran, C.; Jiao, B.; Hou, X.; Duan, X.; Wu, Z. Charge Transport between Coupling Colloidal Perovskite Quantum Dots Assisted by Functional Conjugated Ligands. *Angew. Chem., Int. Ed.* **2018**, *57*, 5754−5758.
(23) De Giorgi, M. L.; Perulli, A.; Yantara, N.; Boix, P. P.; Anni, M. Amplified Spontaneous Emission Properties of Solution Processed $CsPbBr_3$ Perovskite Thin Films. *J. Phys. Chem. C* **2017**, *121*, 14772−14778.
(24) Balena, A.; Perulli, A.; Fernandez, M.; Giorgi, M. L. D.; Nedelcu, G.; Kovalenko, M. V.; Anni, M. Temperature Dependence of the Amplified Spontaneous Emission from $CsPbBr_3$ Nanocrystal Thin Films. *J. Phys. Chem. C* **2018**, *122*, 5813−5819.
(25) Hu, Z.; Liu, Z.; Bian, Y.; Liu, D.; Tang, X.; Hu, W.; Zang, Z.; Zhou, M.; Sun, L.; Tang, J.; Li, Y.; Du, J.; Leng, Y. Robust Cesium Lead Halide Perovskite Microcubes for Frequency Upconversion Lasing. *Adv. Opt. Mater.* **2017**, *5*, No. 1700419.
(26) Song, J.; Li, J.; Li, X.; Xu, L.; Dong, Y.; Zeng, H. Quantum Dot Light-Emitting Diodes Based on Inorganic Perovskite Cesium Lead Halides ($CsPbX_3$). *Adv. Mater.* **2015**, *27*, 7162−7167.
(27) Yuan, S.; Wang, Z.; Zhuo, M.; Tian, Q.; Jin, Y.; Liao, L. Self-Assembled High Quality $CsPbBr_3$ Quantum Dot Films toward Highly Efficient Light-Emitting Diodes. *ACS Nano* **2018**, *12*, 9541−9548.
(28) Wang, Y.; Li, X.; Song, J.; Xiao, L.; Zeng, H.; Sun, H. All-Inorganic Colloidal Perovskite Quantum Dots: A New Class of Lasing Materials with Favorable Characteristics. *Adv. Mater.* **2015**, *27*, 7101−7108.
(29) Yakunin, S.; Protesescu, L.; Krieg, F.; Bodnarchuk, M. I.; Nedelcu, G.; Humer, M.; Luca, G. D.; Fiebig, M.; Heiss, W.; Kovalenko, M. V. Low-Threshold Amplified Spontaneous Emission and Lasing from Colloidal Nanocrystals of Caesium Lead Halide Perovskites. *Nat. Commun.* **2015**, *6*, No. 8056.
(30) Wang, Y.; Li, X. M.; Nalla, V.; Zeng, H. B.; Sun, H. D. Solution-Processed Low Threshold Vertical Cavity Surface Emitting Lasers from All-Inorganic Perovskite Nanocrystals. *Adv. Funct. Mater.* **2017**, *27*, No. 1605088.
(31) Chen, S.; Nurmikko, A. Stable Green Perovskite Vertical-Cavity Surface-Emitting Lasers on Rigid and Flexible Substrates. *ACS Photonics* **2017**, *4*, 2486−2494.
(32) Huang, C. Y.; Zou, C.; Mao, C. Y.; Corp, K. L.; Yao, Y. C.; Lee, Y. J.; Schlenker, C. W.; Jen, A. K. Y.; Lin, L. Y. $CsPbBr_3$ Perovskite Quantum Dot Vertical Cavity Lasers with Low Threshold and High Stability. *ACS Photonics* **2017**, *4*, 2281−2289.
(33) Stranks, S. D.; Wood, S. M.; Wojciechowski, K.; Deschler, F.; Saliba, M.; Khandelwal, H.; Patel, J. B.; Elston, S. J.; Herz, L. M.; Johnston, M. B.; Schenning, A. P. H. J.; Debije, M. G.; Riede, M. K.; Morris, S. M.; Snaith, H. J. Enhanced Amplified Spontaneous Emission in Perovskite Using a Flexible Cholesteric Liquid Crystal Reflector. *Nano Lett.* **2015**, *15*, 4935−4941.
(34) Yoshikawa, T.; Kosaka, H.; Kurihara, K.; Kajita, M.; Sugimoto, Y.; Kasahara, K. Complete Polarization Control of 8×8 Vertical-cavity Surface-emitting Laser Matrix Arrays. *Appl. Phys. Lett.* **1995**, *66*, 908−910.
(35) Li, J.; Shan, X.; Bade, S. G.; Geske, T.; Jiang, Q.; Yang, X.; Yu, Z. Single-Layer Halide Perovskite Light-Emitting Diodes with Sub-Band Gap Turn-On Voltage and High Brightness. *J. Phys. Chem. Lett.* **2016**, *7*, 4059−4066.
(36) Eaton, S. W.; Lai, M.; Gibson, N. A.; Wong, A. B.; Dou, L.; Ma, J.; Wang, L. W.; Leone, S. R.; Yang, P. Lasing in Robust Cesium Lead Halide Perovskite Nanowires. *Proc. Natl. Acad. Sci. USA* **2016**, *113*, 1993−1998.
(37) Li, C.; Zang, Z.; Han, C.; Hu, Z.; Tang, X.; Du, J.; Leng, Y.; Sun, K. Enhanced Random Lasing Emission from Highly Compact $CsPbBr_3$ Perovskite Thin Films Decorated by ZnO Nanoparticles. *Nano Energy* **2017**, *40*, 195−202.
(38) Yantara, N.; Bhaumik, S.; Yan, F.; Sabba, D.; Dewi, H. A.; Mathews, N.; Boix, P. P.; Demir, H. V.; Mhaisalkar, S. Inorganic Halide Perovskites for Efficient Light-Emitting Diodes. *J. Phys. Chem. Lett.* **2015**, *6*, 4360−4364.
(39) Tang, X.; Hu, Z.; Chen, W.; Xing, X.; Zang, Z.; Hu, W.; Qiu, J.; Du, J.; Leng, Y.; Jiang, X.; Mai, L. Room Temperature Single-Photon Emission and Lasing for All-Inorganic Colloidal Perovskite Quantum Dots. *Nano Energy* **2016**, *28*, 462−468.
(40) Fu, Y.; Zhu, H.; Stoumpos, C. C.; Ding, Q.; Wang, J.; Kanatzidis, M. G.; Zhu, X.; Jin, S. Broad Wavelength Tunable Robust

DOI: 10.1021/acsami.8b15962
ACS Appl. Mater. Interfaces 2018, 10, 40661−40671

Lasing from Single-Crystal Nanowires of Cesium Lead Halide Perovskites ($CsPbX_3$, X= Cl, Br, I). *ACS Nano* **2016**, *10*, 7963−7972.
(41) Wei, Z.; Perumal, A.; Su, R.; Sushant, S.; Xing, J.; Zhang, Q.; Tan, S. T.; Demir, H. V.; Xiong, Q. Solution-Processed Highly Bright and Durable Cesium Lead Halide Perovskite Light-Emitting Diodes. *Nanoscale* **2016**, *8*, 18021−18026.
(42) Chen, S.; Zhang, C.; Lee, J.; Han, J.; Nurmikko, A. High-Q, Low-Threshold Monolithic Perovskite Thin-Film Vertical-Cavity Lasers. *Adv. Mater.* **2017**, *29*, No. 1604781.
(43) Veldhuis, S. A.; Boix, P. P.; Yantara, N.; Li, M. J.; Sum, T. C.; Mathews, N.; Mhaisalkar, S. G. Perovskite Materials for Light-Emitting Diodes and Lasers. *Adv. Mater.* **2016**, *28*, 6804−6834.
(44) Ma, Q.; Huang, S.; Wen, X.; Green, M. A.; Ho-Baillie, A. W. Y. Hole Transport Layer Free Inorganic $CsPbIBr_2$ Perovskite Solar Cell by Dual Source Thermal Evaporation. *Adv. Energy Mater.* **2016**, *6*, No. 1502202.
(45) Yong, Z. J.; Zhou, Y.; Ma, J.; Chen, Y.; Yang, J.; Song, Y.; Wang, J.; Sun, H. Controlling Crystallization of All-Inorganic Perovskite Films for Ultralow-Threshold Amplification Spontaneous Emission. *ACS Appl. Mater. Interfaces* **2017**, *9*, 32920−32929.
(46) Liu, M.; Johnston, M. B.; Snaith, H. J. Efficient Planar Heterojunction Perovskite Solar Cells by Vapour Deposition. *Nature* **2013**, *501*, 395−398.
(47) Conings, B.; Baeten, L.; De, D. C.; D'Haen, J.; Manca, J.; Boyen, H. G. Perovskite-Based Hybrid Solar Cells Exceeding 10% Efficiency with High Reproducibility Using a Thin Film Sandwich Approach. *Adv. Mater.* **2014**, *26*, 2041−2046.
(48) Xu, Y.; Chen, Q.; Zhang, C.; Wang, R.; Wu, H.; Zhang, X.; Xing, G.; Yu, W. W.; Wang, X.; Zhang, Y.; et al. Two-Photon-Pumped Perovskite Semiconductor Nanocrystal Lasers. *J. Am. Chem. Soc.* **2016**, *138*, 3761−3768.
(49) Hu, Y.; Wang, Q.; Shi, Y.; Li, M.; Zhang, L.; Wang, Z.; Liao, L. Vacuum-Evaporated All-Inorganic Cesium Lead Bromine Perovskites for High-Performance Light-Emitting Diodes. *J. Mater. Chem. C* **2017**, *5*, 8144−8149.
(50) Zhang, X.; Xu, B.; Zhang, J.; Gao, Y.; Zheng, Y.; Wang, K.; Sun, X. W. All-Inorganic Perovskite Nanocrystals for High-Efficiency Light Emitting Diodes: Dual-Phase $CsPbBr_3$-$CsPb_2Br_5$ Composites. *Adv. Funct. Mater.* **2016**, *26*, 4595−4600.
(51) Ling, Y.; Tan, L.; Wang, X.; Zhou, Y.; Xin, Y.; Ma, B.; Hanson, K.; Gao, H. W. Composite Perovskites of Cesium Lead Bromide for Optimized Photoluminescence. *J. Phys. Chem. Lett.* **2017**, *8*, 3266−3271.
(52) Frolova, L. A.; Anokhin, D. V.; Piryazev, A. A.; Luchkin, S. Y.; Dremova, N. N.; Stevenson, K. J.; Troshin, P. A. Highly Efficient All-Inorganic Planar Heterojunction Perovskite Solar Cells Produced by Thermal Coevaporation of CsI and PbI_2. *J. Phys. Chem. Lett.* **2017**, *8*, 67−72.
(53) Nikl, M.; Nitsch, K.; Chval, J.; Somma, F.; Phani, A. R.; Santucci, S.; Giampaolo, C.; Fabeni, P.; Pazzi, G. P.; Feng, X. Q. Optical and Structural Properties of Ternary Nanoaggregates in CsI-PbI_2 Co-Evaporated Thin Films. *J. Phys.: Condens. Matter* **2000**, *12*, 1939−1946.
(54) Moody, G.; Dass, C. K.; Hao, K.; Chen, C. H.; Li, L. J.; Singh, A.; Tran, K.; Clark, G.; Xu, X.; Berghauser, G.; Malic, E.; Knorr, A.; Li, X. Intrinsic Homogeneous Linewidth and Broadening Mechanisms of Excitons in Monolayer Transition Metal Dichalcogenides. *Nat. Commun.* **2015**, *6*, No. 8315.
(55) Li, X.; Wu, Y.; Zhang, S.; Cai, B.; Gu, Y.; Song, J.; Zeng, H. Quantum Dots: $CsPbX_3$ Quantum Dots for Lighting and Displays: Room-Temperature Synthesis, Photoluminescence Superiorities, Underlying Origins and White Light-Emitting Diodes. *Adv. Funct. Mater.* **2016**, *26*, 2584.
(56) Roman, B. J.; Otto, J.; Galik, C.; Downing, R.; Sheldon, M. Au Exchange or Au Deposition: Dual Reaction Pathways in Au-$CsPbBr_3$ Heterostructure Nanoparticles. *Nano Lett.* **2017**, *17*, 5561−5566.
(57) Lehner, A. J.; Fabini, D. H.; Evans, H. A.; Hébert, C. A.; Smock, S. R.; Hu, J.; Wang, H.; Zwanziger, J. W.; Chabinyc, M. L.; Seshadri, R. Crystal and Electronic Structures of Complex Bismuth Iodides $A_3Bi_2I_9$ (A = K, Rb, Cs) Related to Perovskite: Aiding the Rational Design of Photovoltaics. *Chem. Mater.* **2015**, *27*, 7137−7148.
(58) Kao, T. S.; Chou, Y. H.; Chou, C. H.; Chen, F. C.; et al. Lasing Behaviors upon Phase Transition in Solution-Processed Perovskite Thin Films. *Appl. Phys. Lett.* **2014**, *105*, No. 231108.
(59) Leyden, M. R.; Matsushima, T.; Qin, C.; Ruan, S.; Ye, H.; Adachi, C. Amplified Spontaneous Emission in Phenylethylammonium Methylammonium Lead Iodide Quasi-2D Perovskites. *Phys. Chem. Chem. Phys.* **2018**, *20*, 15030.
(60) D' Innocenzo, V.; Grancini, G.; Alcocer, M. J.; Kandada, A. R.; Stranks, S. D.; Lee, M. M.; Lanzani, G.; Snaith, H. J.; Petrozza, A. Excitons Versus Free Charges in Organo-Lead Tri-Halide Perovskites. *Nat. Commun.* **2014**, *5*, No. 3586.
(61) Dhanker, R.; Brigeman, A. N.; Larsen, A. V.; Stewart, R. J.; Asbury, J. B.; Giebink, N. C. Random Lasing in Organo-Lead Halide Perovskite Microcrystal Networks. *Appl. Phys. Lett.* **2014**, *105*, No. 151112.
(62) Dang, C.; Nurmikko, A. Beyond Quantum Dot LEDs: Optical Gain and Laser Action in Red, Green, and Blue Colors. *MRS Bull.* **2013**, *38*, 737−742.
(63) Shaklee, K. L.; Leheny, R. F. Direct Determination of Optical Gain in Semiconductor Crystals. *Appl. Phys. Lett.* **1971**, *18*, 475−477.
(64) Klimov, V. I.; Mikhailovsky, A. A.; Xu, S.; Malko, A.; Hollingsworth, J. A.; Leatherdale, C. A.; Bawendi, M. G.; et al. Optical Gain and Stimulated Emission in Nanocrystal Quantum Dots. *Science* **2000**, *290*, 314−317.
(65) Dang, C.; Lee, J.; Breen, C.; Steckel, J. S.; Coesullivan, S.; Nurmikko, A. Red, Green and Blue Lasing Enabled by Single-Exciton Gain in Colloidal Quantum Dot Films. *Nat. Nanotechnol.* **2012**, *7*, 335−339.
(66) Wang, R.; Tong, Y.; Manzi, A.; Wang, K.; Fu, Z.; Kentzinger, E.; Feldmann, J.; Urban, A. S.; Buschbaum, P. M.; Frielinghaus, H. Preferential Orientation of Crystals Induced by Incorporation of Organic Ligands in Mixed-Dimensional Hybrid Perovskite Films. *Adv. Opt. Mater.* **2018**, *6*, No. 1701311.
(67) Chen, W.; Zhang, J.; Xu, G.; Xue, R.; Li, Y.; Zhou, Y.; Hou, J.; Li, Y. A Semitransparent Inorganic Perovskite Film for Overcoming Ultraviolet Light Instability of Organic Solar Cells and Achieving 14.03% Efficiency. *Adv. Mater.* **2018**, *30*, No. 1800855.
(68) Marra, D. C.; Aydil, E. S.; Joo, S. J.; Yoon, E.; Srdanov, V. I. Angle-Dependent Photoluminescence Spectra of Hydrogenated Amorphous Silicon Thin Films. *Appl. Phys. Lett.* **2000**, *77*, 3346−3348.

DOI: 10.1021/acsami.8b15962
ACS Appl. Mater. Interfaces 2018, 10, 40661−40671